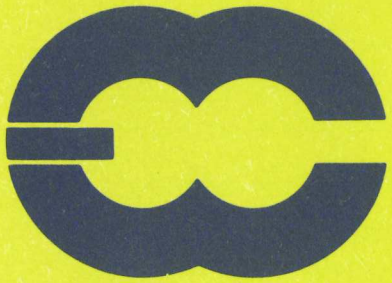

European Centre
for Medium Range
Weather Forecasts

A channel version of the ECMWF Gridpoint Model

Internal Report No. 16
Research Dept.

December 77

Centre Européen pour les Prévisions Météorologiques
à Moyen Terme

Europäisches Zentrum für mittelfristige Wettervorhersage

1. Introduction

A channel version of the adiabatic part of the ECMWF gridpoint model has been developed for the purpose of examining the development of barotropically and baroclinically unstable waves in simple zonal flows. The model itself is described by Burridge & Haseler (1977) and Haseler & Burridge (1977), and the reader is referred to these reports for details. The present report describes the modifications for the channel (Section 2), the generation of initial flows (Section 3) and some integrations with low vertical resolution (Section 4).
All notations and symbols used here are those found in the global model descriptions. However, for simplicity, the spherical coordinates, (λ,θ) have been replaced by Cartesian (x,y).

2. Modifications for the channel

The global, latitude-longitude grid, model has been converted to channel geometry by replacing the poles with fixed, impermeable walls. The walls are placed at v-points in the Arakawa C grid (see Figure 2.1). In the east-west the cyclic boundaries of the global model are retained. Apart from changes necessitated by the walls, the global code remains unchanged. The channel model can thus be run with spherical geometry, if one so wishes with a Fourier filter to increase the maximum CFL-stable timestep. β-plane geometry is obtained by changing some "map-factors", i.e. some latitude dependent constants. This means that some unnecessary multiplications are performed, but the advantage is that we can use exactly the same numerical formulations as in the spherical model.

The boundary conditions at the lateral walls are zero normal winds and zero normal mass fluxes

$$v = 0 \quad \text{at NROW=1, NROW=MAXROW} \tag{2.1}$$
$$V = 0 \tag{2.2}$$

An additional boundary condition is needed for the potential vorticity

$$Z = \frac{1}{p_s}\left[f + \frac{\partial v}{\partial x} - \frac{\partial u}{\partial y}\right]$$

at the wall-points (Fig. 2.1). Obviously $\left(\frac{\partial v}{\partial x}\right)$ is zero here, but the computation of $\left(\frac{\partial u}{\partial y}\right)$ requires an assumption. The natural choice would be

$$\left(\frac{\partial u}{\partial y}\right)_1 = 2\left(\frac{\partial u}{\partial y}\right)_2 - \left(\frac{\partial u}{\partial y}\right)_3 \tag{2.3}$$

with a corresponding expression at the southern wall. With the present I/O configuration of the global model, $\left(\frac{\partial u}{\partial y}\right)_3$ is however not available when needed, and we have used the simpler condition

$$\left(\frac{\partial u}{\partial y}\right)_1 = \left(\frac{\partial u}{\partial y}\right)_2 \tag{2.4}$$

This formulation generates noise near the walls, which in the form of small scale divergence waves slowly moves perpendicularly towards the centre of the channel. After a few days they contaminate the whole area. At present the problem is suppressed with a moderate linear diffusion everywhere, the diffusion coefficient set to $K = 10^5 m^2 s^{-1}$ when $\Delta y = 100$ km. A final elimination of the boundary induced noise would probably require a reformulation of the boundary condition (2.4).

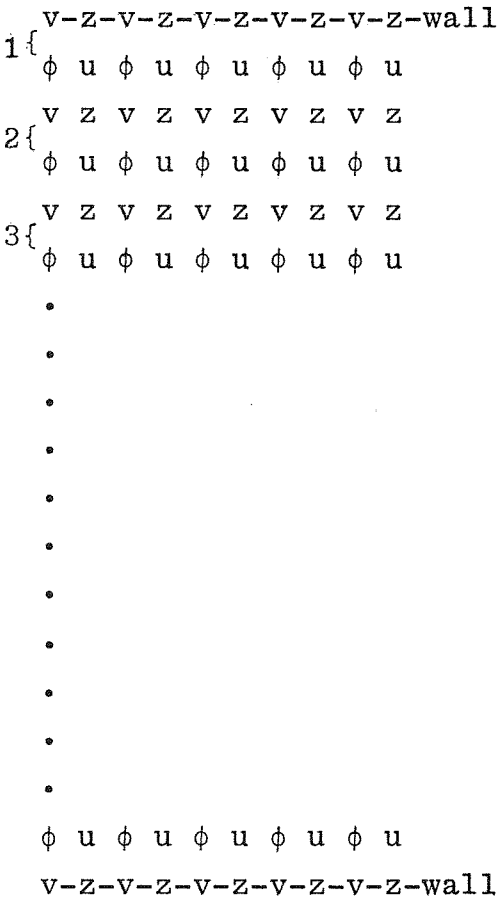

Figure 2.1 The grid of the channel version. The walls are marked with thick lines.

Alternatively a simpler formulation of the rotational terms $[ZV]_2$ and $[ZU]_1$ in the momentum equations, that does not require Z at the walls, could be tried.

3. Initial data

For the channel experiments we intended to prescribe the windfield exactly and compute a balanced mass field directly from the balance equation in σ-coordinates. This procedure would allow us to choose simple, analytically generated basic flows of the types that are used in theoretical studies of barotropic or baroclinic instability. Hoskins & Simmons (1975) describe a procedure whereby this is achieved in their spectral model. They solve the reverse balance equation at each level, using predefined winds, giving NLEV equations for NLEV temperatures, one at each level. An extra equation is however required to close the system since there are NLEV+1 unknowns, the NLEV temperatures T_k, (k=1, NLEV) and the surface pressure p_s. Hoskins and Simmons tried extrapolation from the lowest temperature level down to the surface, but with this method they obtained vertical 2-$\Delta\sigma$-waves in the balanced temperatures. Instead they used an artificial smoothing equation to eliminate the noise and at the same time close the system. This technique was also tried in our gridpoint model.

The procedure is the following :

$$\frac{\partial u}{\partial t} + A_u + \overline{\frac{\partial \phi}{\partial x}}^{\sigma} + RT \frac{\partial \ln p_s}{\partial x} = 0 \qquad (3.1)$$

$$\frac{\partial v}{\partial t} + A_v + \overline{\frac{\partial \phi}{\partial y}}^{\sigma} + RT \frac{\partial \ln p_s}{\partial y} = 0$$

A_u and A_v contain the advective and rotational terms.

Forming the balance equation we get

$$\nabla^2\bar{\phi}^{\sigma} + RT\nabla^2 \ln p_s + R\left(\frac{\partial T}{\partial x}\frac{\partial \ln p_s}{\partial x} + \frac{\partial T}{\partial y}\frac{\partial \ln p_s}{\partial y}\right) = -\nabla \cdot A \qquad (3.3)$$

Here $A = A_u\, i + A_v\, j$ is calculated directly by the forecast code by putting $T_k = 0$, $\ln p_s = 0$ and making a one timestep forecast. The advantage is that the balance equation uses the same finite difference expressions as the forecast model.

In equation (3.3) the temperature is divided into two parts

$$T(x,y,\sigma) = \tilde{T}(\sigma) + T'(x,y,\sigma)$$

where $\tilde{T}(\sigma)$ is the ICAO-atmosphere.
By moving all terms containing T' to the right hand side (r.h.s.), we get a Poisson equation at each level,k.

$$\nabla^2(\bar{\phi}_k^{\sigma} + R\tilde{T}_k \ln p_s) = \text{r.h.s.} \qquad (3.4)$$

This equation needs lateral boundary conditions, and they may be obtained by assuming geostrophic winds close to the walls, where we thus have the Neumann conditions

$$\frac{\partial}{\partial y}\left(\bar{\phi}_k^{\sigma} + R\tilde{T}_k \ln p_s\right) = -f\bar{u}_k^{xy} - \frac{\partial}{\partial y}\left(RT_k' \ln p_s\right) \qquad (3.5)$$

NROW=2

NROW=MAXROW-1

Assuming an initial guess for T_k' in (3.4) and (3.5) the Poisson equation can be solved. This is done by a direct FFT Poisson solver supplied by C.Temperton at ECMWF.

In the centre of the channel the temperature structure is defined as

$$T_k = \tilde{T}_k$$

and the deviations from this basic state at other latitudes are obtained from the solutions of the balance equation.

$$\overline{\phi}_k^{\sigma} + R\tilde{T}_k \ln p_s = \nabla^{-2}(\text{r.h.s.}) \qquad (3.6)$$

together with the hydrostatic equations

$$\left(\frac{\Delta_\sigma \phi}{\Delta_\sigma (\ln\sigma)}\right)_k = - RT_k \qquad (3.7)$$

and the smoothing equation

$$\sum \gamma_k T_k = 0 \qquad (3.8)$$

In equation (3.8) the γ_k are numerical coefficients, chosen by Hoskins and Simmons as the binominal coefficients with alternating signs. Thus for a 5-level model γ_k is given by

$$\gamma_k = (1,-4,6,-4,1)$$

(3.6), (3.7) and (3.8) give an approximate solution of T_k and p_s. The procedure is iterated with $(T_k - \tilde{T}_k)$ as a new guess of T_k' to put in (r.h.s.). The convergence is very rapid, only a few iterations are needed to obtain temperature deviations less than 0.01 Kelvin.

In low vertical resolution, NLEV=5, the procedure is fairly successful, see Figures(3.1a) and (3.1b). In Figure (3.1a) the balanced temperature profiles close to the two lateral walls, as well as the predefined temperatures at the centre of the channel, are shown. The zonal wind profile in this case was determined by

$$\frac{du}{d\ln\sigma} = -19 \text{ ms}^{-1}$$

which gives the zonal winds plotted in the figure. The temperatures obtained are relatively smooth, however the lowest, NLEV=5, temperature is a little colder than expected.

With a somewhat more realistic zonal wind profile, increasing up to the tropopause at $\sigma=.3$ and constant thereafter, the balanced temperatures are those in Figure (3.1b). Here the lowest level temperatures differ considerably from those of an anticipated smooth profile; the northern being too cold and the southern too warm. Indeed, with sharper tropopauses, the lowest layer even becomes superadiabatic close to the southern wall. These deviations from a smooth profile can be interpreted as reflexions of the, real, temperature "kink" at the tropopause caused by the filtering procedure. The filter (3.8) removes the $2\Delta\sigma$-component of the kink, leaving $3\Delta\sigma$ and longer components to remain visible as deviations.

In higher vertical resolutions, NLEV=20, the balancing procedure is completely unsatisfactory. In Figure (3.2a) the balancing is done in pressure coordinates, where the system of equations is closed and no artificial equation of type (3.8) is needed. A large amplitude $2\Delta\sigma$ wave is visible in the whole atmosphere.

This is a clear example of the kind of noise that motivated the smoothing used by Hoskins and Simmons. Its origin can be traced back to the particular choice of vertical coordinate systems made. In our case the winds and the temperatures are both defined at the same levels, while the geopotentials are defined at intermediate levels. This requires a vertical averaging in the balance equation

$$\overline{\phi}^{p}_{k} = \nabla^{-2}(\text{r.h.s.}) \tag{3.6b}$$

Using the hydrostatic equation

$$\left(\frac{\Delta_p \phi}{\Delta_p \ln p}\right)_k = - RT_k \tag{3.7b}$$

the temperatures, T_k, can in principle be determined. This, however, turns out to be an algebraically ill-conditioned problem, and an attempt to solve it gives the result in Figure (3.2a). Hoskins and Simmons on the other hand do define the geopotentials and the winds at the same levels, but since their temperatures are also defined at these levels, they have to do a vertical averaging in the hydrostatic equation, again leading to an ill-conditioned problem.

In σ-coordinates, with the smoother (3.8) added, our procedure gives the temperatures in Figure (3.2b). In analogy with the filter used in the 5-level version in Figure (3.1), the coefficients, γ_k , in (3.8) were chosen as the binominal coefficients of order 20. These coefficients are very large in the middle of the atmosphere, but comparatively small elsewhere. In Figure (3.2b) it can be seen that the $2\Delta\sigma$ wave is removed in the vicinity of 500 mb, leaving $3\Delta\sigma$ and longer components. Further up and down, however, the effect of the smoother is minimal.

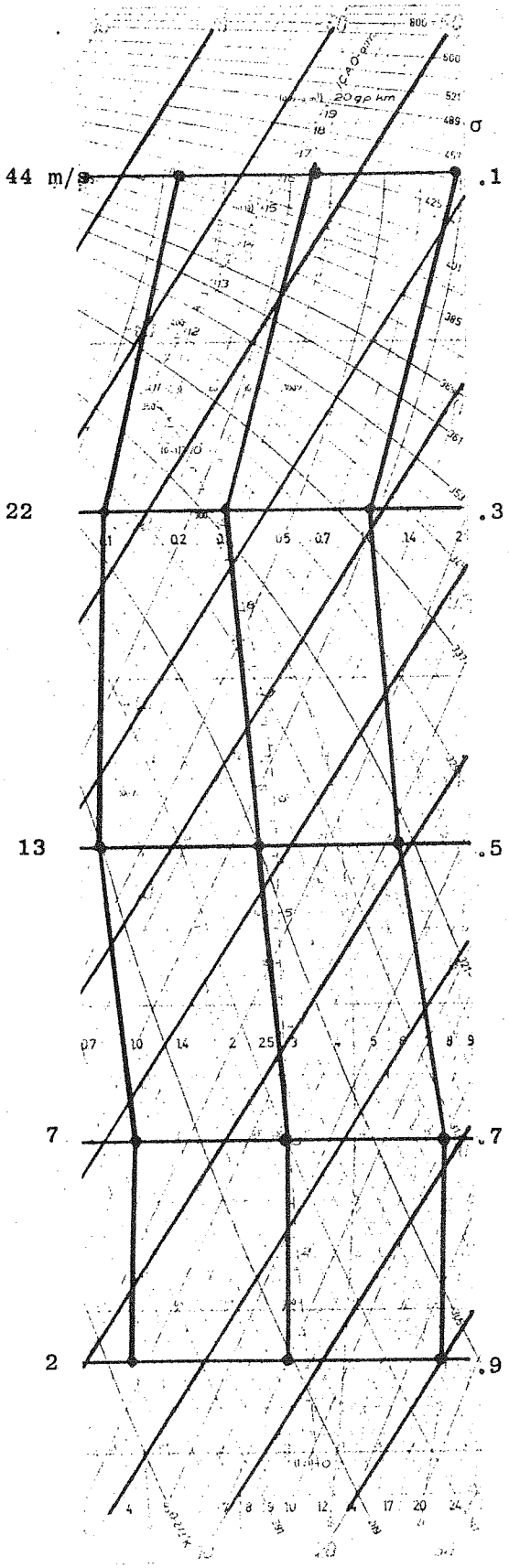

Fig.3.1a Temperatures at north wall, centre and south wall after balancing. Zonal winds from $du/d\ln\sigma = -19$

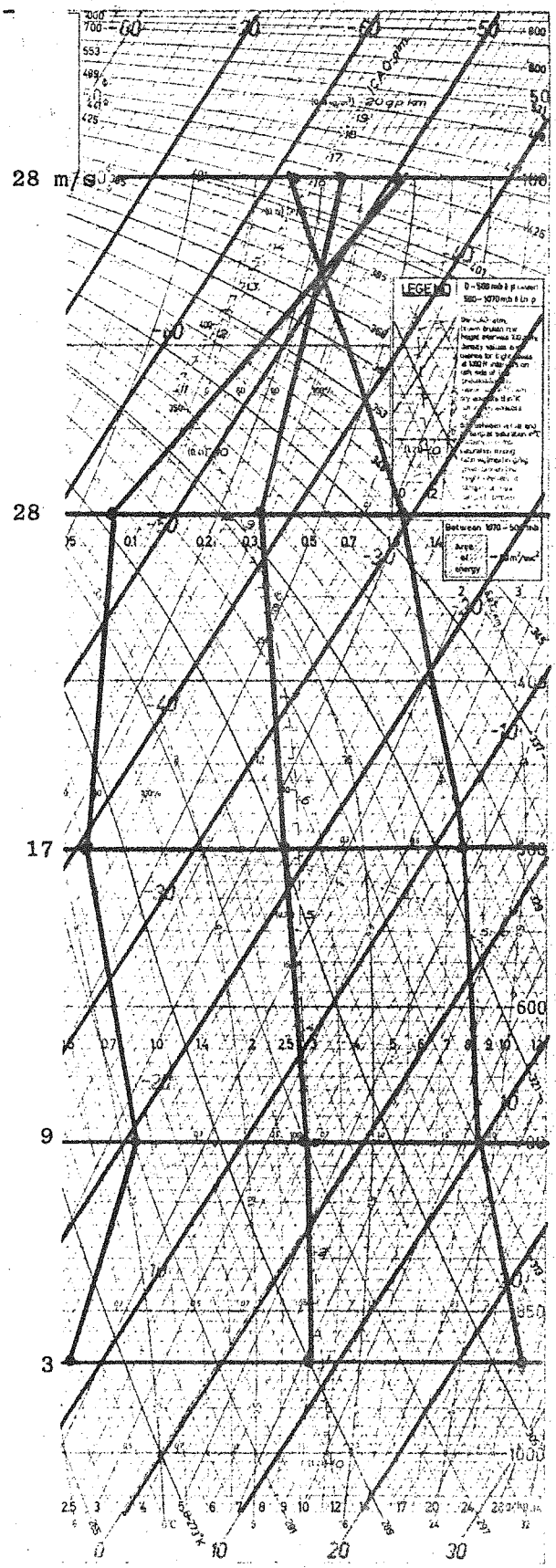

Fig.3.1b As 3.1a, but with constant stratospheric winds.

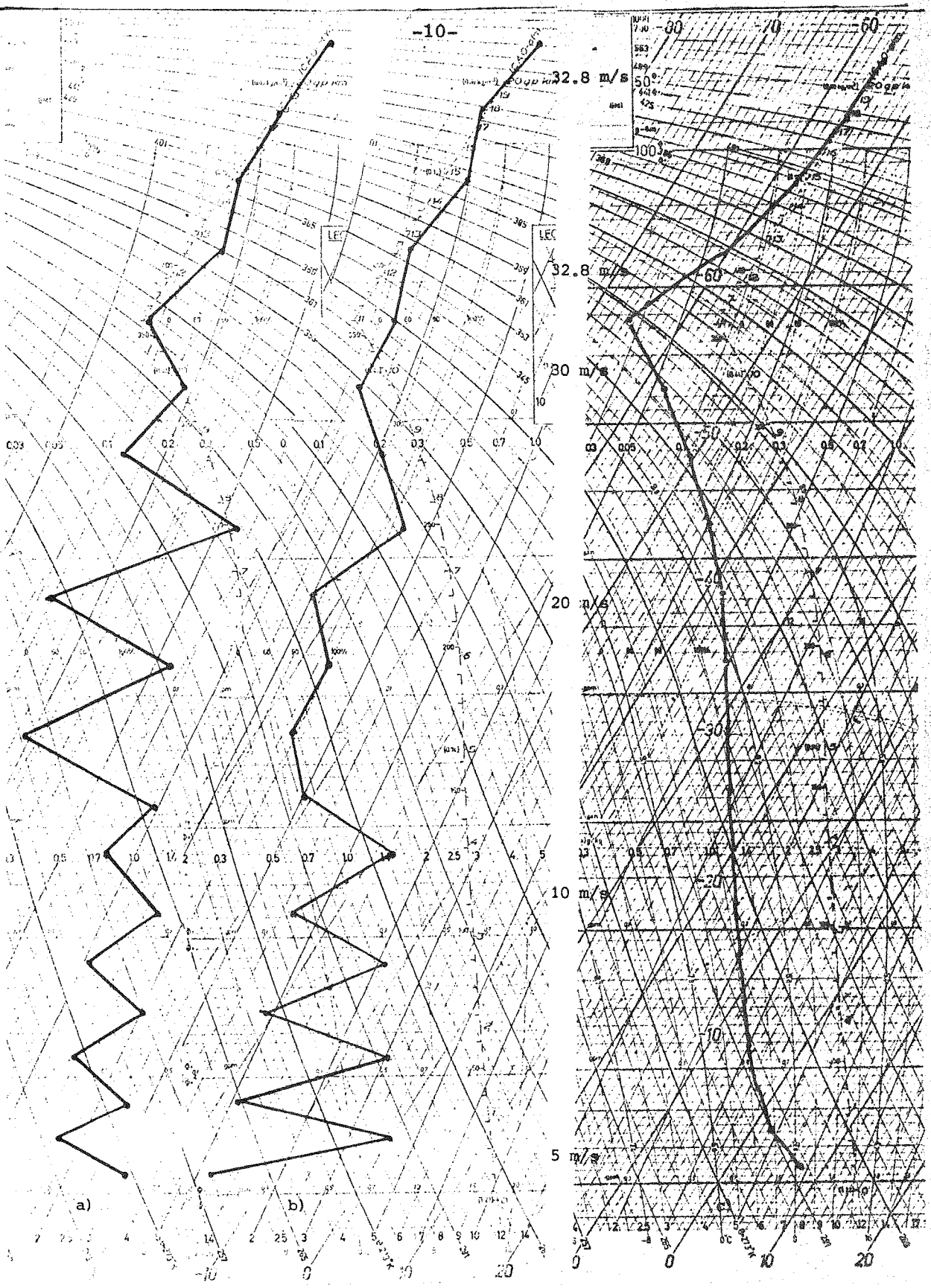

Figure 3.2 Balanced temperatures. Zonal wind du/dlnσ=-19 in troposphere, constant in stratosphere. Curve a) p-system, Curve b) σ-system, Curve c) σ- system without vertical averaging of temperature, see text.

It can be argued that some other smoother, for instance of the Shapiro type, should be used, but since this is still a somewhat artificial way of overcoming the problem, we have instead chosen an initialisation procedure where the problem never arises. By defining the initial winds and geopotentials at the same so-called "half" levels, in the model atmosphere, and the temperatures at the intermediate "full" levels, the sigma-system problem is closed. The reverse balance equation is solved at the half levels, including the earth's surface, which has no orography. This gives NLEV+1 balance equations for the NLEV+1 unknowns, ϕ_k,(k=1,NLEV) and p_s.

The retrieval of the temperatures from the hydrostatic equation (3.7) is now a trivial matter. The full level winds are obtained from the same analytical expression used for the half level winds.

Using this latter procedure the balanced temperatures are perfectly smooth, see Figure (3.2c), and the fields seem to be sufficiently balanced for our purposes according to some preliminary 20-level integrations. In the present report we will however only describe results obtained from the 5-level initial states produced by the method described in connection with Figures 3.1.

4. Some integrations

Integrations of three different basic states will be described here, all of them with the low vertical resolution NLEV=5. The cases will be referred to as "barotropic", "baroclinic" and "barotropic-baroclinic" respectively. In the barotropic case the initial wind varies only meridionally, and the initial temperature is

isothermal, giving a barotropic initial mass field. The baroclinic initial state is characterised by vertical shear in the wind, and a highly baroclinic mass field. Finally in the barotropic-baroclinic case there is both vertical and latitudinal shear in the initial wind. In all three cases a perturbation meridional wind, $v'(x,y,\sigma,o)$ is added to the zonal wind, u. The perturbation is a simple sinusoidal wave

$$v'(x,y,\sigma,o) = v_o \cdot \sin \frac{2\pi}{L_x} (x-\delta) \qquad (4.1)$$

where L_x is the length of the channel. The initial disturbance is thus confined to wave number 1. In all three cases the amplitude $v_o = 1 ms^{-1}$ and the phase, $\delta = 0^o$, at all levels.

The balancing procedure in Section 3 was performed on the total wind field u + v'. Table 4.1 summarises the different runs.

	Shear	Resolution	Wavelength, L_x
Case 1 "barotropic"	$\frac{du}{dy} \neq 0$ (parabolic or $\cos^2$); $\frac{du}{dz} = 0$	$\Delta x = 100$ km; $\Delta y = 200$ km	4000 km
Case 2 "baroclinic"	$\frac{du}{dy} = 0$; $\frac{du}{dz} \neq 0$	$\Delta x = 100$ km; $\Delta y = 100$ km	2000 km
Case 3 "barotropic-baroclinic"	$\frac{du}{dy} \neq 0$; $\frac{du}{dz} \neq 0$	$\Delta x = 100$ km or 200 km; $\Delta y = 100$ km	2000 km or 4000 km

Table 4.1

The channel width was 3200 km in all cases. The five sigma-levels were equidistant with the "full" levels at σ = .1, .3, .5, .7 and .9 respectively.
The area was 20 x 33 points. β-plane geometry with the channel centre at the latitude 45^{o} was used throughout. In some of the integrations a "southern hemisphere" β -plane was used in order to check for possible coding errors in connection with the boundary induced noise. The explicit timestep, finally, was usually 75 seconds. In order to suppress the temporal computational mode generated by the leap-frog scheme, a weak time filter of the Asselin type was applied. In order to interpret the integrations, a Fourier analysis was made of all the forecast fields every second hour, and amplitudes and phases of the wave numbers 0 to 8 were determined at all levels.

4.1 The barotropic case

Kuo (1951) showed that, in order for a zonal jet to be barotropically unstable, a necessary requirement is that the zonal wind, u, satisfies the condition

$$\beta - \frac{d^2u}{dy^2} = 0 \qquad (4.2)$$

at least once within the width of the jet.
A simple analytic shape of a jet that satisfies the condition is

$$u = u_o \cdot \cos^2\left(\frac{\pi}{L_y}(y-y_o)\right) \qquad (4.3)$$

where y_o is the centre of the channel. When $\beta = 1.6 \cdot 10^{-11}$ $m^{-1}s^{-1}$, and L_y = 2000 km this $\cos^2$-shaped jet is barotropically unstable already with $u_o = 4ms^{-1}$. On the other hand a parabolic jet-profile

$$u = u_o \cdot \left(1-\left[\frac{y-y_o}{0.5L_y}\right]^2\right) \qquad (4.4)$$

does not satisfy (4.2) for any value of u_o, and should be barotropically stable.

The two cases (4.3) and (4.4) were integrated up to 5 days. Linear diffusion with the diffusion coefficient $k = 10^5\ m^2s^{-1}$ was included,but in order to keep the barotropy of the atmosphere, the surface friction in the model was eliminated.

As expected, the parabolic jet, (4.4) was stable up to day 5. Figure (4.1) shows the amplitude of wave number 1 of the v-component at level $\sigma = .5$. Only small amplitude gravity waves, originating from the small remaining imbalance in the initialised mass and wind fields, can be observed. The diffusion dampens these waves, and at day 5 their amplitude is of the order of a few tenths of a ms^{-1}.
The $\cos^2$ -shaped jet (4.3) was on the other hand highly unstable. As in the parabolic case, $u_o = 40ms^{-1}$, which is a rather large value compared to that necessary for instability according to the condition (4.2). Figure (4.2) shows the growth of wave number 1 of the v-component with time in a logarithmic diagram. The amplitude grows almost exactly exponentially from day 1 to day 4. From day 0 to day 1 there is an adjustment period during which the most unstable barotropic mode emerges from the initial perturbation. After day 4 the slope of the growth rate curve flattens due to non-linear effects.
The wave number 2 amplitude of the zonal wind component, u, is still only a few tenths of a ms^{-1}at day $3\frac{1}{2}$, but has grown to $2ms^{-1}$ at day 5. The slope of the linear part of the growth curve corresponds to a growth rate of $7.3 \cdot 10^{-6}s^{-1}$, corresponding to an e-folding time of 1.6 days. Even if the initial state was barotropic, the

model itself is of course fully baroclinic, and nothing prevents baroclinic developments to take place. An examination of the forecast wind fields at day 5 shows that the flow is still barotropic to a very high degree. No differences can be detected between the $\sigma=.1$ and $\sigma=.9$ wind fields. Neither does the Fourier analysis reveal any non-barotropic features.

Yanai and Nitta (1968) studied instability in a linearised barotropic model without divergence. Sub-dividing the latitudinal dimension into finite differences, they used the method of linear perturbations to determine the stability properties of small amplitude waves in the flow. The phase velocities and amplitudes of the possible modes were obtained from the eigenvalues and eigenvectors of a matrix, dependent on the flow characteristics and the Rossby parameter, β.
With a latitudinal resolution of N=20, and the same zonal wind profile and perturbation wavelength as in our case, they obtained a growth rate of the most unstable mode of $7.10^{-6}sec^{-1}$ ($\sim$1.7 days e-folding time). Yanai and Nitta also determined the latitudinal structure of the unstable mode as a function of, among other things, the horizontal finite difference resolution. Further comparisons with the gridpoint model are planned, but have not yet been completed.

4.2 The baroclinic case

The vertical shear in the baroclinic case was defined as

$$\frac{du}{d\ln\sigma} = -19 \ ms^{-1} \qquad (4.5)$$

which gives the zonal winds shown in Figure (3.1a), which also shows the temperature structure of the initial state.

Linear diffusion ($k=10^5 m^2 s^{-1}$), dry convective adjustment (never called into action in the actual runs) and surface friction of the drag coefficient type, $C_d = 0.02$, were the only "physical" effects included.

A 2000-km wave was integrated up to 6 days. As in the barotropic case, some time is needed for the most unstable mode to emerge from the initial perturbation, defined by equation (4.1), in this case almost two days. The wave then grows exponentially to day 6, when the integration was stopped. The slope of the growth rate curve corresponds to an e-folding time of about 2.8 days, see Figure (4.3). The vertical structure of the wave number 1 Fourier components of meridional wind and temperature are shown in Figure (4.4). The most obvious feature is the shallowness of the wave, already at $\sigma = .5$ the temperature wave is virtually absent. The v-wave tilts westward with height, about 50^o between $\sigma = .9$ and $\sigma = .3$, with most of the tilt in the lowest layer. At $\sigma = .1$ there is hardly any v-wave left. The temperature wave, on the other hand, tilts eastward with height within the lowest layer, and is virtually absent higher up.
These features agree well with observed short wave disturbances on the polar front.

Song (1971) among many others, has investigated the stability properties of different "baroclinic" and "barotropic-baroclinic" basic states. He used a balanced, linearised model and , using the same technique as Yanai and Nitta, he divided the latitudinal and vertical coordinates into finite difference increments. The characteristics of small amplitude wave perturbations were then determined with the eigen-mode method. For a wave with the same dimensions as

ours and with 15 vertical levels, he obtained an e-folding time of about 3 days. The basic zonal flow used by Song differed from ours, he used a climatological profile as opposed to our equation (4.5). The vertical structrue of Song's 2000-km wave has been normalised and plotted as a dotted line in Figure (4.3). We can see that the agreement is good, the differences are certainly attributable to the higher vertical resolution in Song's case.

4.3 The barotropic-baroclinic case

Two runs, one with a 2000-km wave and the other with a 4000-km wave will be described here. In both of them, the meridional profile of the initial jet-stream was of the $\cos^2$- type, equation (4.3). In the vertical $du/d\ln\sigma = -19ms^{-1}$ (Figure 3.1a) for the 4000-km wave, while u varied "climatologically" with sigma (Figure 3.1b) for the 2000-km wave.
Judging from the results of Section 4.1, the 4000-km wave should be highly barotropically unstable, particularly at the top level, $\sigma = .1$, where u_o was $44ms^{-1}$. Indeed the top level wave moves almost independently of the lower levels, where baroclinic development takes place. Figure (4.5) shows the growth rates in this case at the two levels $\sigma = .1$ and $\sigma = .7$. We can note that neither of the waves grows exponentially during any prolonged time, but there seems to be some interaction between the growth rates. When the top level wave grows most rapidly around day 3 to 4 the low level wave is only exhibiting minimal growth. Around day 6, when the top level wave grows very slowly, the low level wave starts growing. At day 8 the situation is again reversed. In Figure (4.6) the vertical structure is displayed for days 3,5,7 and 9. These figures confirm that in the lower half of the atmosphere

a typical baroclinic disturbance, with backward tilt of the wind field and forward tilt of the temperature field has developed. At the top level one can only note that the phase of the, large amplitude, v-wave is not locked to the low level wave, but moves independently with a phase speed determined solely by $u(\sigma=.1)$ and β. The temperature perturbation at level $\sigma=.1$ does not grow in proportion to the wind perturbation. In conclusion there seem to be two processes going on simultaneously, with a fairly complicated flow as the result.

The 2000-km wave on the other hand should be barotropically stable in spite of the $\cos^2$-profile. Yanai and Nitta show in their paper that with our dimensions of the jet, there is a short wave cut-off of barotropic instability somewhere around 2500 km. This case is thus in most respects identical to that of Section 4.2. Since the baroclinicity and the zonal flow reached all the way from the channel centre to the walls in that case, the unsatisfactory lateral boundary conditions mentioned in Section 2, caused noise generation close to the walls in that case, and the maps produced were contaminated with small scale noise. With the $\cos^2$-jet, on the other hand, conditions close to the walls are calm and the linear diffusion can kill the noise with only a small diffusion coefficient.
This case was then integrated to 10 days, with the wave number 1 v-component reaching a maximum amplitude around day 6, Figure (4.7). Non-linear effects become noticeable around day 4, and the wave is dampened after day 7. The amplitude of the surface pressure wave shows the same picture, Figure (4.8), with a maximum low around day 6 which subsequently fills out. A run without diffusion up to day 8 is also plotted in this figure. In that case the wave grows faster and reaches a deeper minimum already

at day 5, whereafter the filling process is also more rapid.
Figure (4.9) shows the vertical structure of the 2000-km wave at days 0, 3, 6 and 9. Day 3 is during the most rapid growth phase, day 6 at the maximum amplitude, and day 9 during the decay phase. We can notice that the westward tilt with height is largest, about 50^{o} between σ=.9 and σ=.3, during the rapid growth at day 3. Already at the mature state, day 6, the tilt has decreased, and during the decay at day 9 the wind wave is virtually vertical. The wind wave amplitude shows two maxima, one at σ=.9 and the other at σ=.5. The temperature wave tilts forward with height in the lower atmosphere, and is again virtually absent above σ=.5.

Finally, some illustrations of the disturbance at its maximum amplitude around day 6 are shown. Figures (4.10a), (4.10b) and (4.10c) show the surface pressure, the lowest level (σ=.9) winds and the lowest level temperatures respectively. Figure (4.10d) is a superposition of the three previous maps. The relative vorticity at σ =.9 is shown in Figure (4.11) and the divergence at σ=.7 in Figure (4.12). We can see that a realistically looking middle latitude cyclone has developed. Due to the short wavelength chosen for the initial disturbance it is very shallow, as has already been discussed. There is a closed surface low with an extended trough stretching towards south and south-west. The "900-mb" winds are relatively geostrophic, but a certain amount of frictional cross-isobar flow can be observed. The highest wind speeds are observed in the north-westerlies behind the low and the southerlies ahead of it. The "900-mb" temperatures show a distinct warm sector protruding from the south towards the centre of the low. There is a zone of large temperature gradient to the north and east

of the warm sector, and another sharp temperature gradient behind it in the south-west. These zones of large temperature gradients are connected with zones of maximum relative vorticity, and they are thus typical warm and cold fronts respectively. By subjective measure the warm front appears to be somewhat sharper than the cold front, a feature that has been noted in previous numerical simulations of mid-latitude cyclones. Behind the cold front there is a broad outflow of cold air, with low level divergence. Low level convergence is observed ahead of the warm front and in a narrow zone just at the cold front. At the upper levels, $\sigma=.5$ and $\sigma=.3$ the divergence pattern is reversed with divergence above the warm front and convergence above the cold outflow. This is of course the divergence distribution necessary for the observed distribution of vertical velocities in a mid-latitude cyclone. Within the limitations of 5 vertical levels, and, in particular, no moisture or latent heat release and a very crude horizontal diffusion, the cyclone is reassuringly realistic.

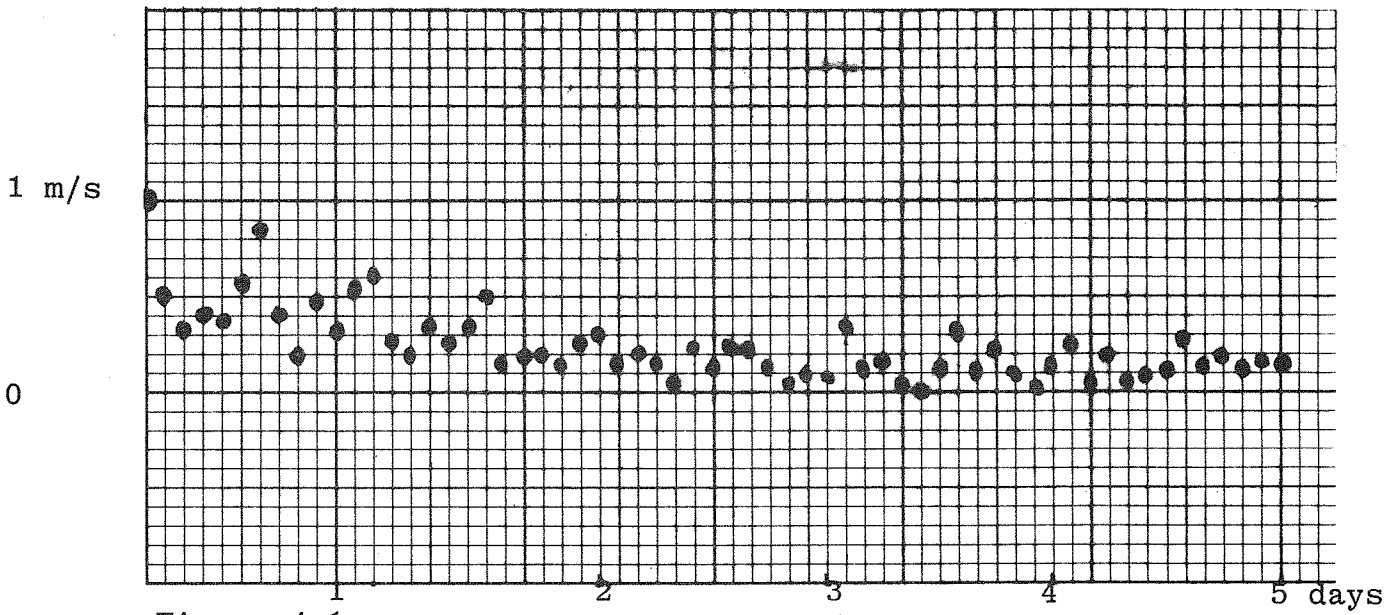

Figure 4.1 Amplitude of wavenumber 1, v-wave.
Barotropic case, parabolic jet

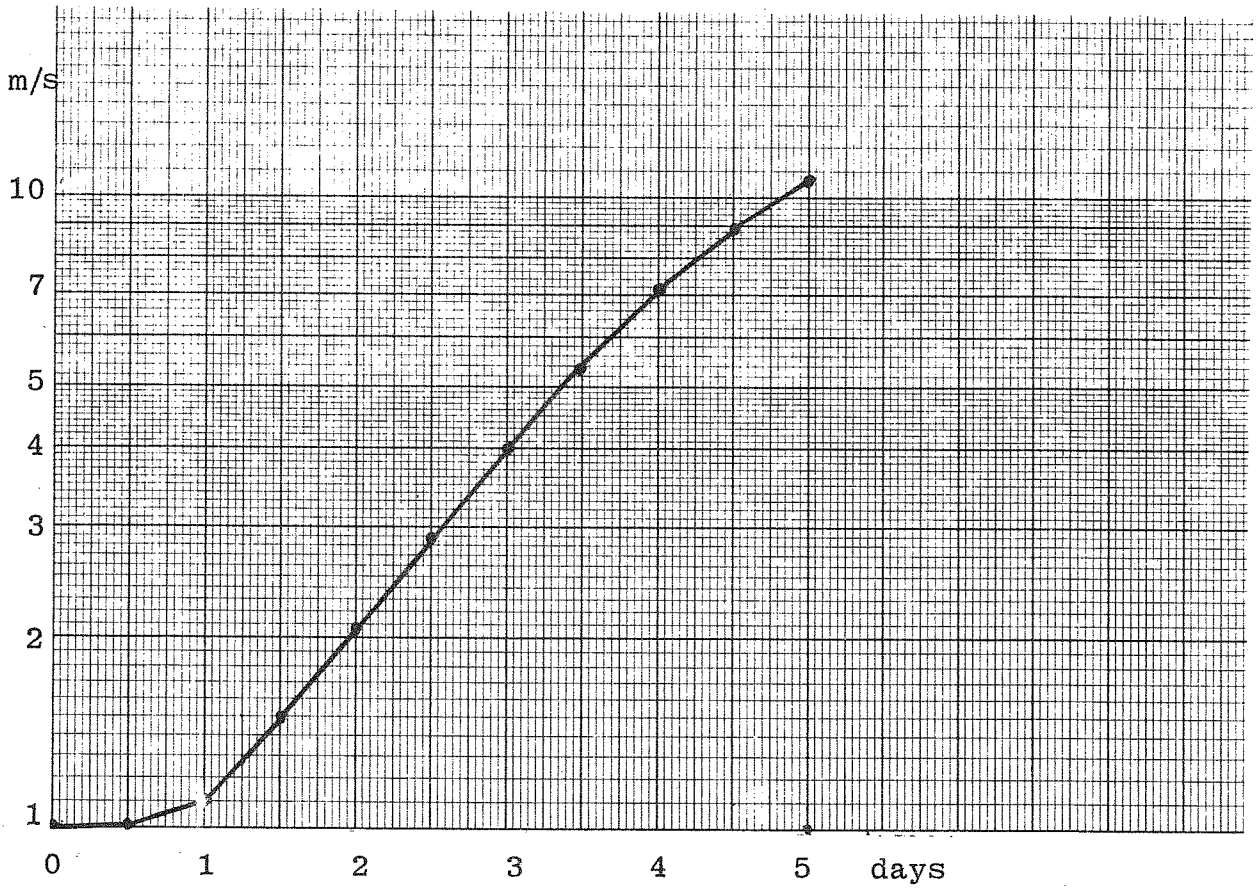

Figure 4.2 Amplitude of wavenumber 1, v-wave.
Barotropic case, $\cos^2$-jet.

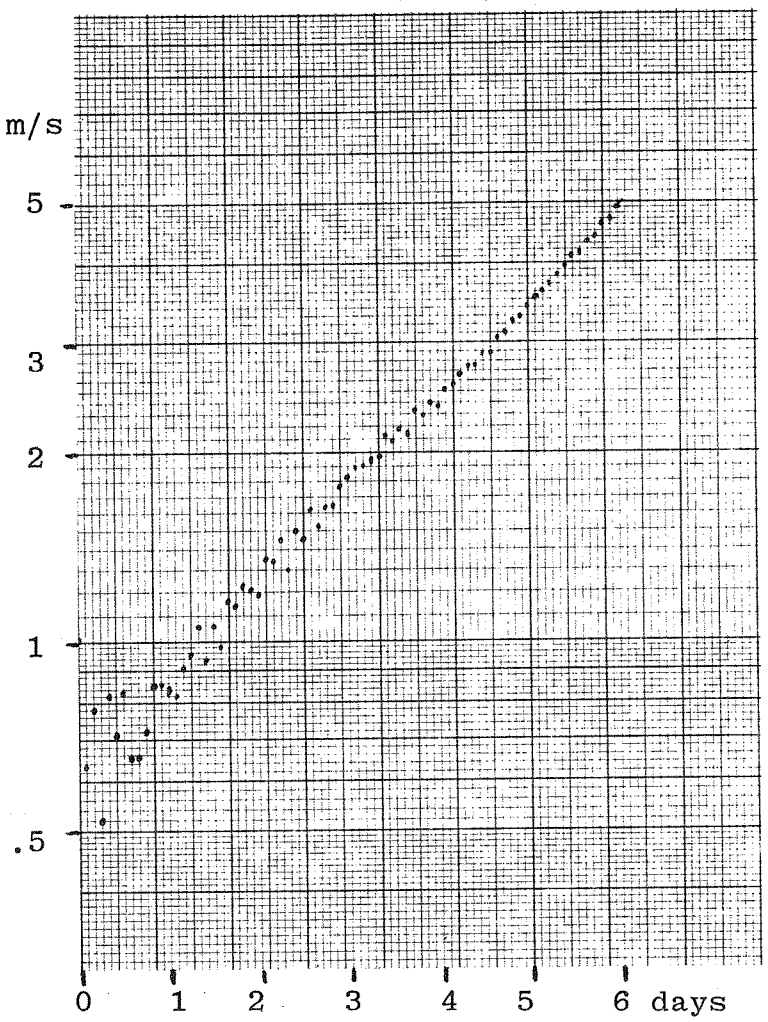

Figure 4.3

Amplitude of wavenumber 1, v-wave. σ =.7. Baroclinic case L_x=2000 km

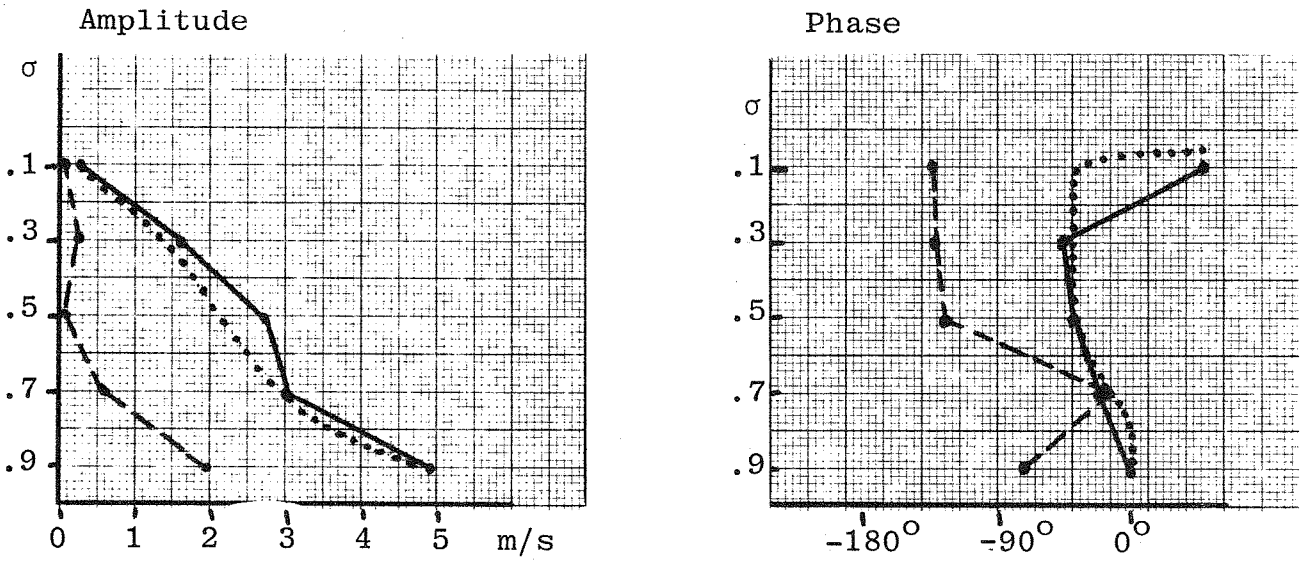

Figure 4.4 Amplitude and phase of wavenumber 1, v-wave (full line) and T-wave (dashed line). Baroclinic case. The dotted lines show the corresponding curves from Song's work.

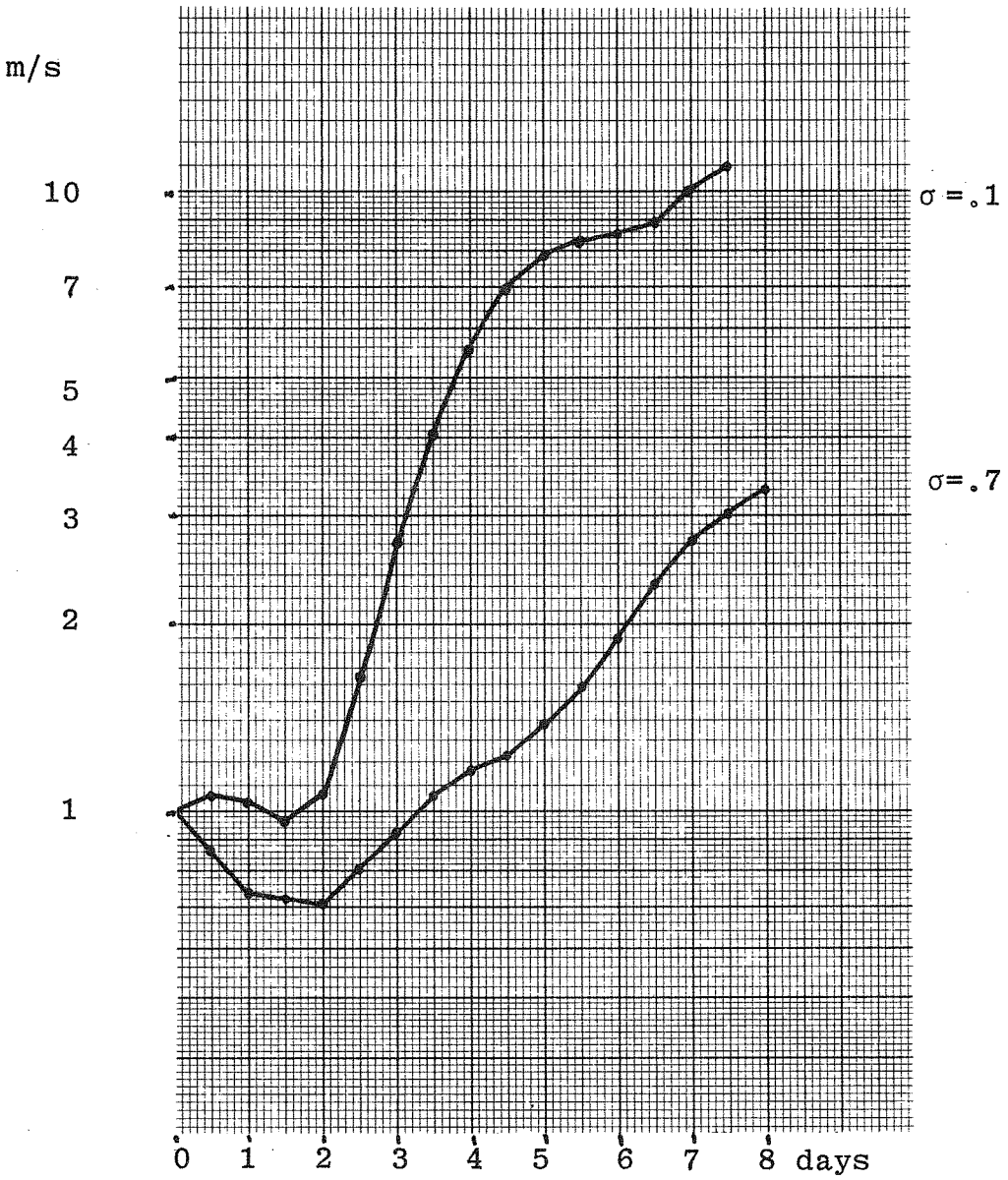

Figure 4.5 Amplitudes of wavenumber 1, v-wave at σ=.1 and σ=.7. Barotropic-Baroclinic case L_x=4000 km.

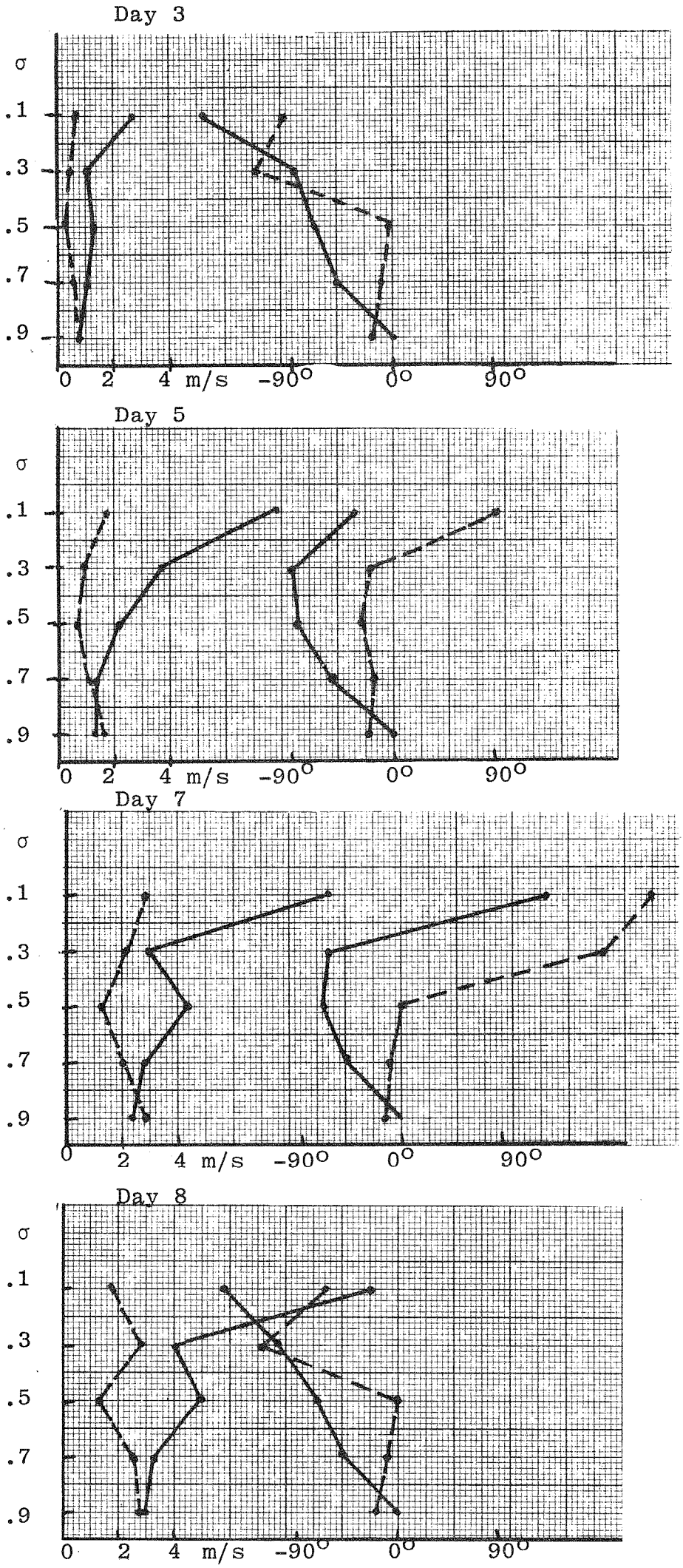

Figure 4.6

Amplitudes and phases of wave-number 1, v-wave (full line) and T-wave (dahsed). Barotropic-Baroclinic case, L_x=4000 km

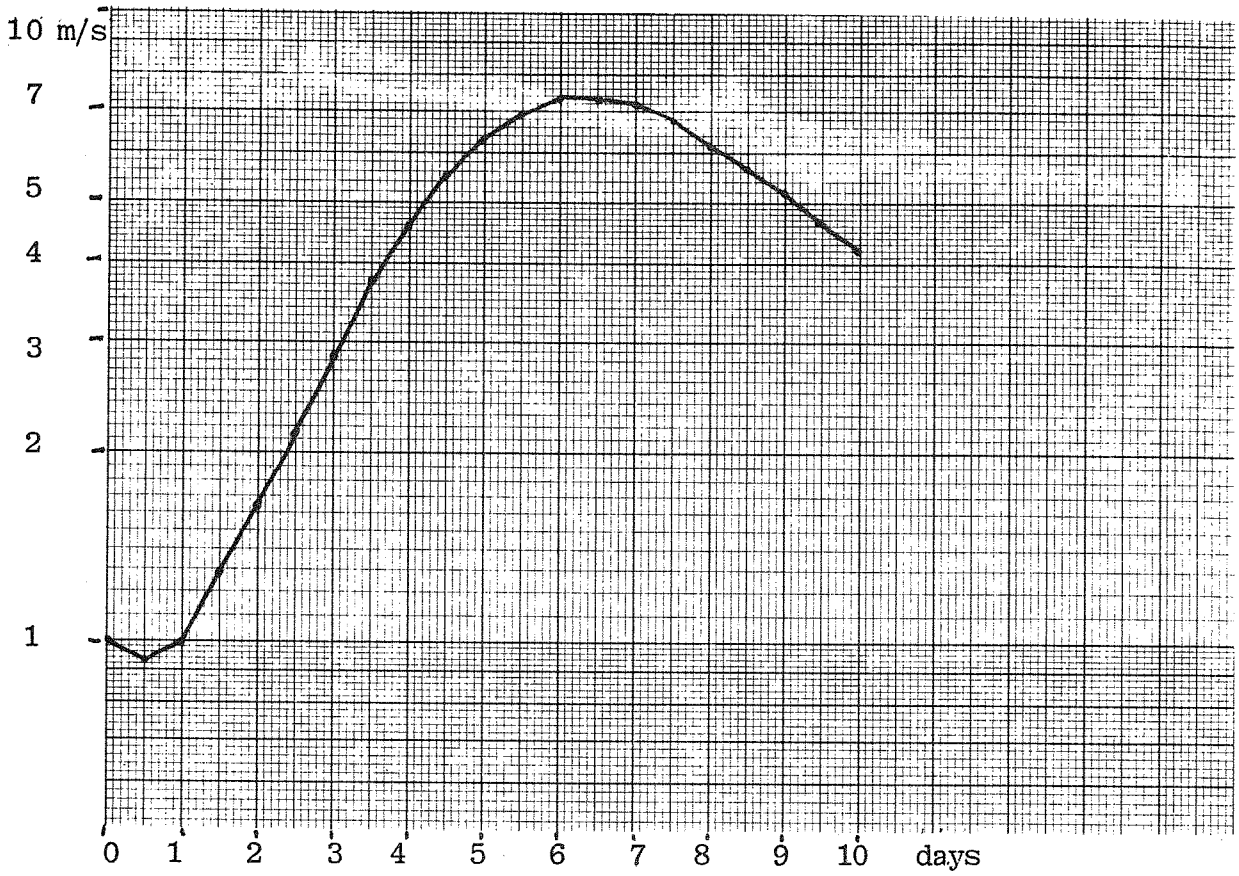

Figure 4.7 Amplitude of wavenumber 1, v-wave σ=.7
Barotropic-Baroclinic L_x=2000 km

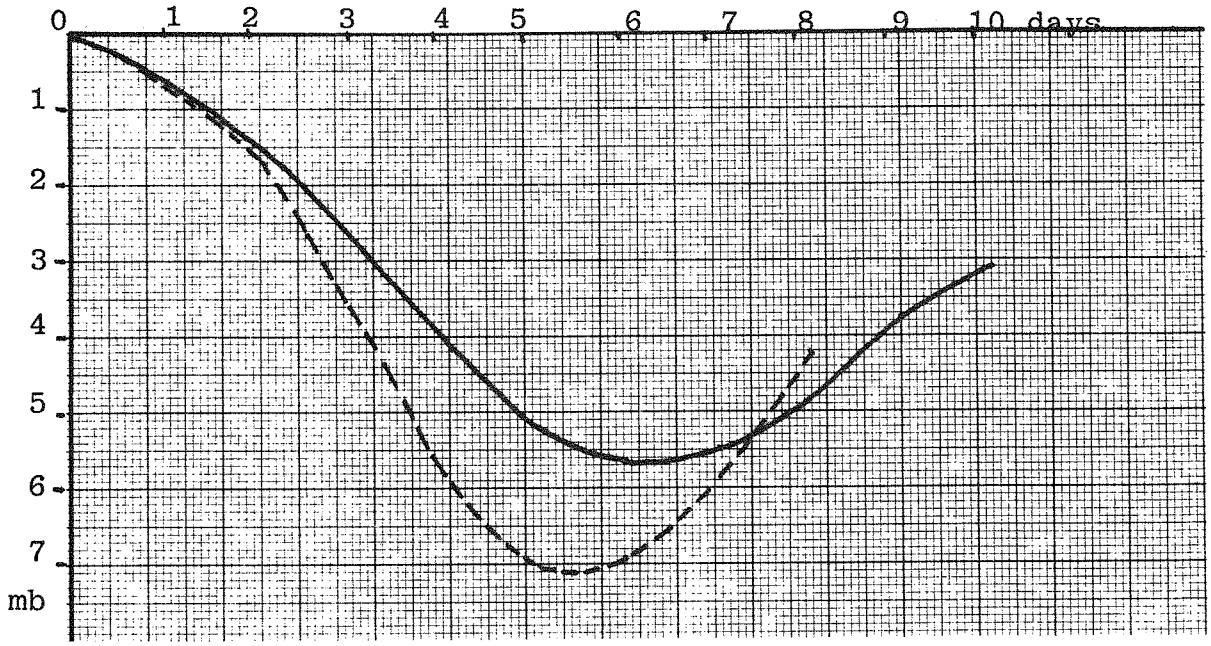

Figure 4.8 Amplitude of wavenumber 1, surface pressure.
Barotropic-Baroclinic case.
Diffusion coefficient, k=0. (dashed) and
$k=10^5$ (full line).

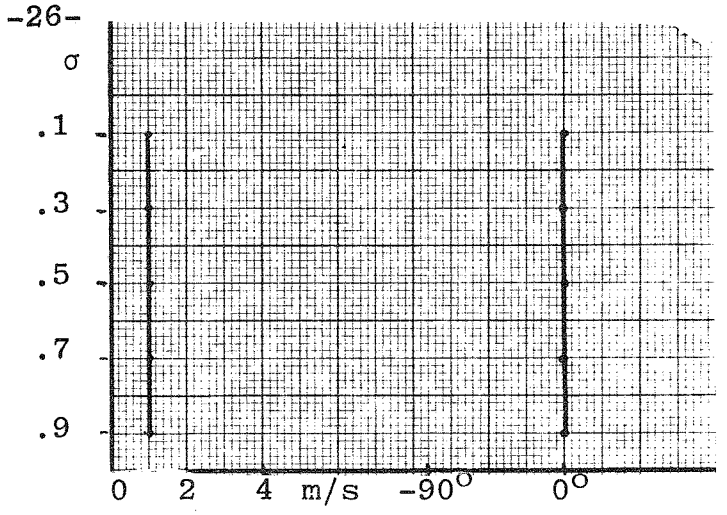

Day 0

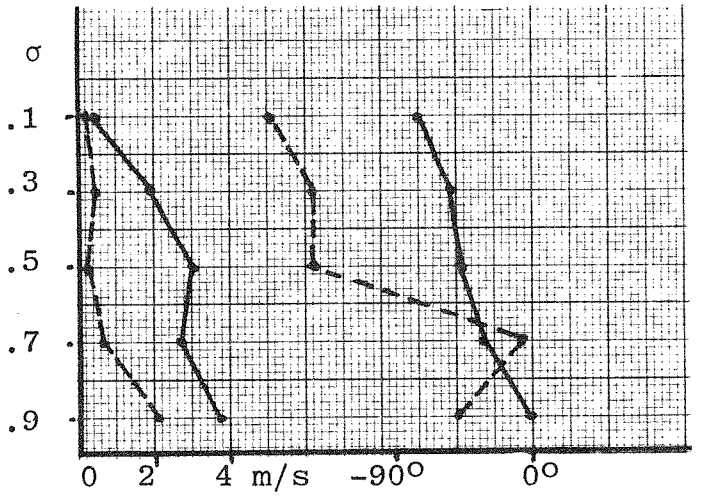

Day 3

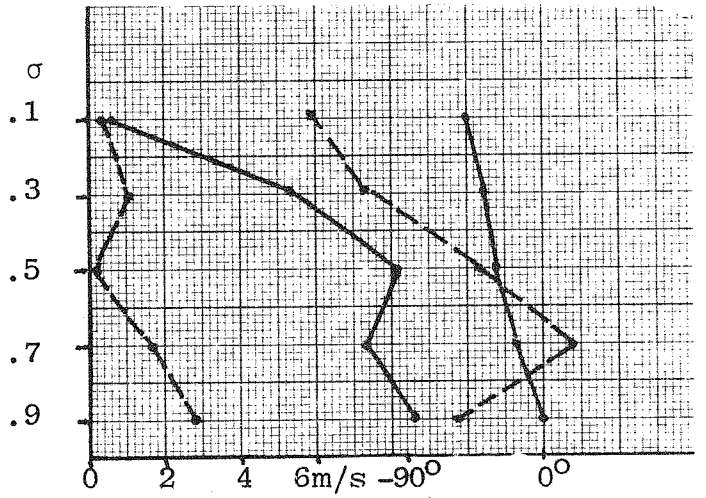

Day 6

Figure 4.9 Amplitudes and phases wavenumber 1, v-wave (full line) and T-wave (dashed) Barotropic-Baroclinic L_x=2000 km

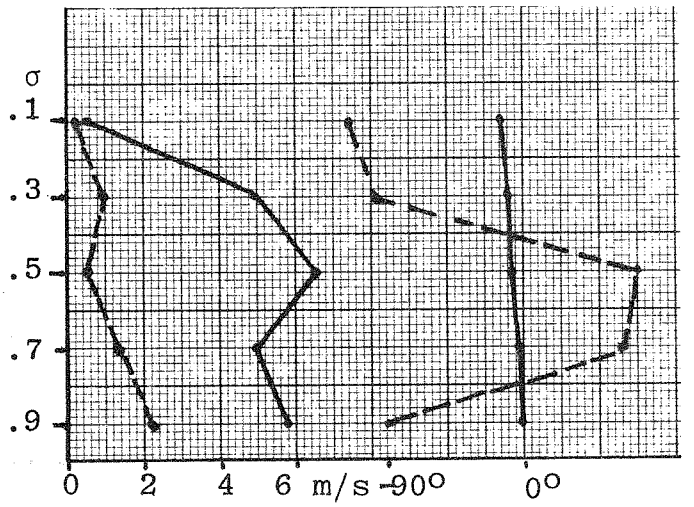

Day 9

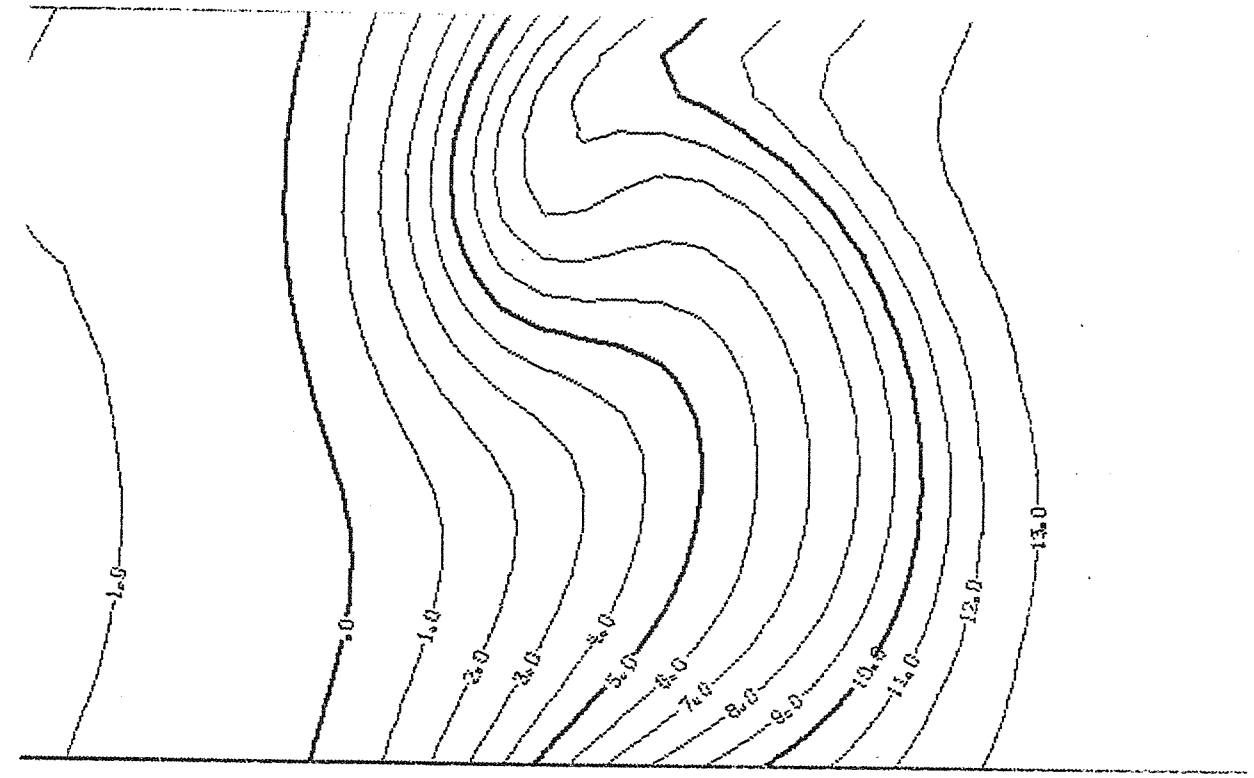

Fig. 4.10b Temperature (^{o}C)at σ=.9, day 6

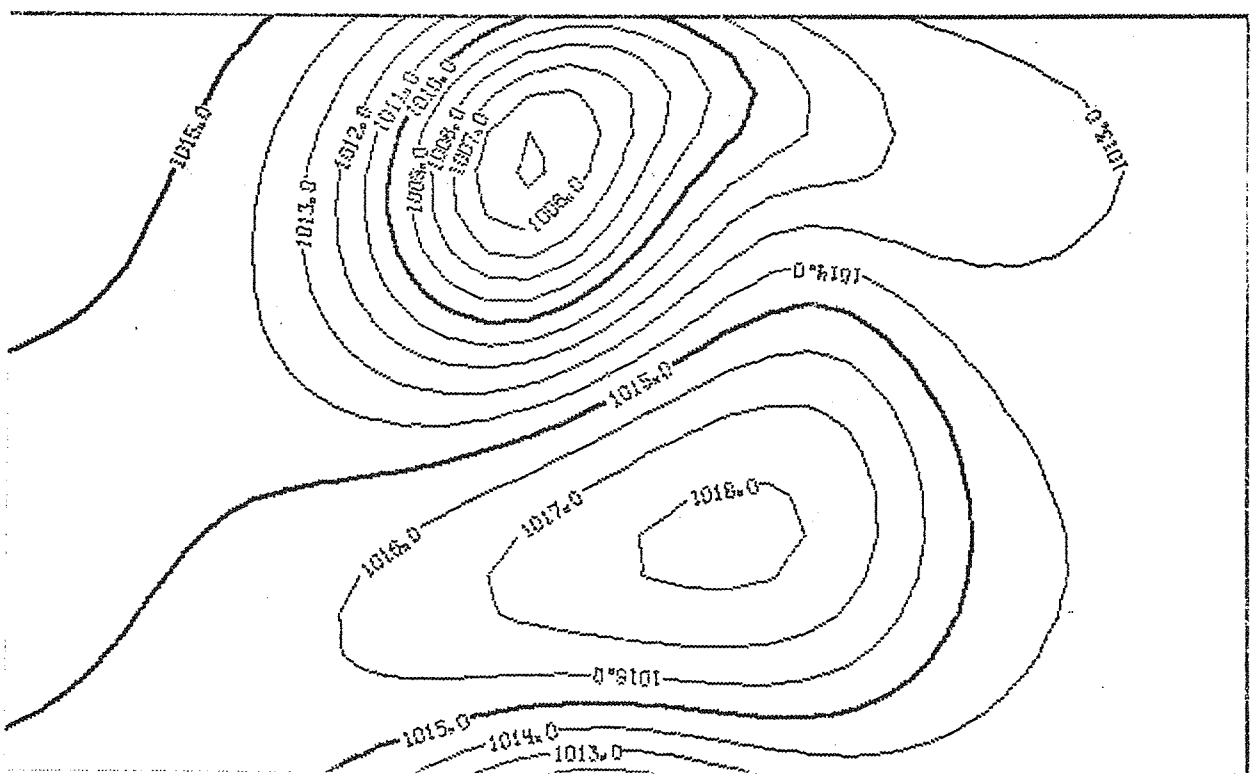

Fig. 4.10a Surface pressure (mb) at day 6

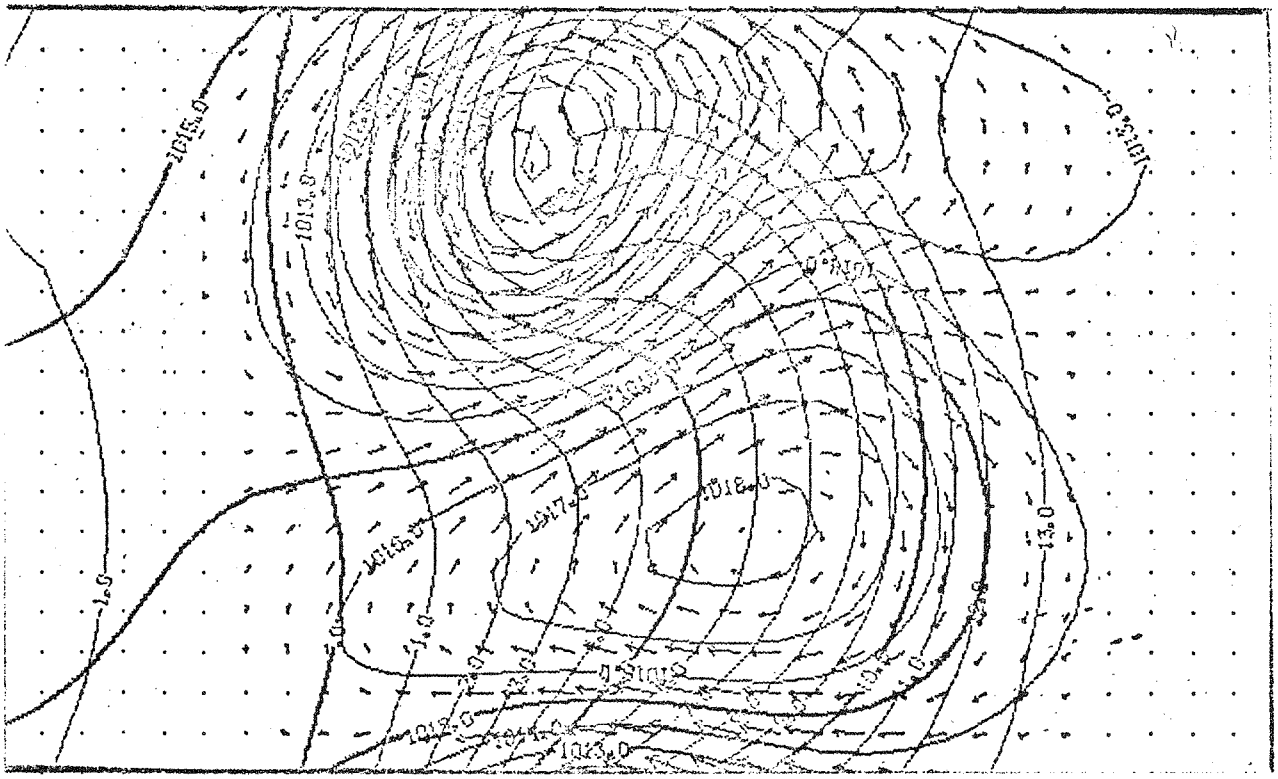

Fig. 4.10d Superposition of figures 4.10 a, 4.10 b and 4.10 c.

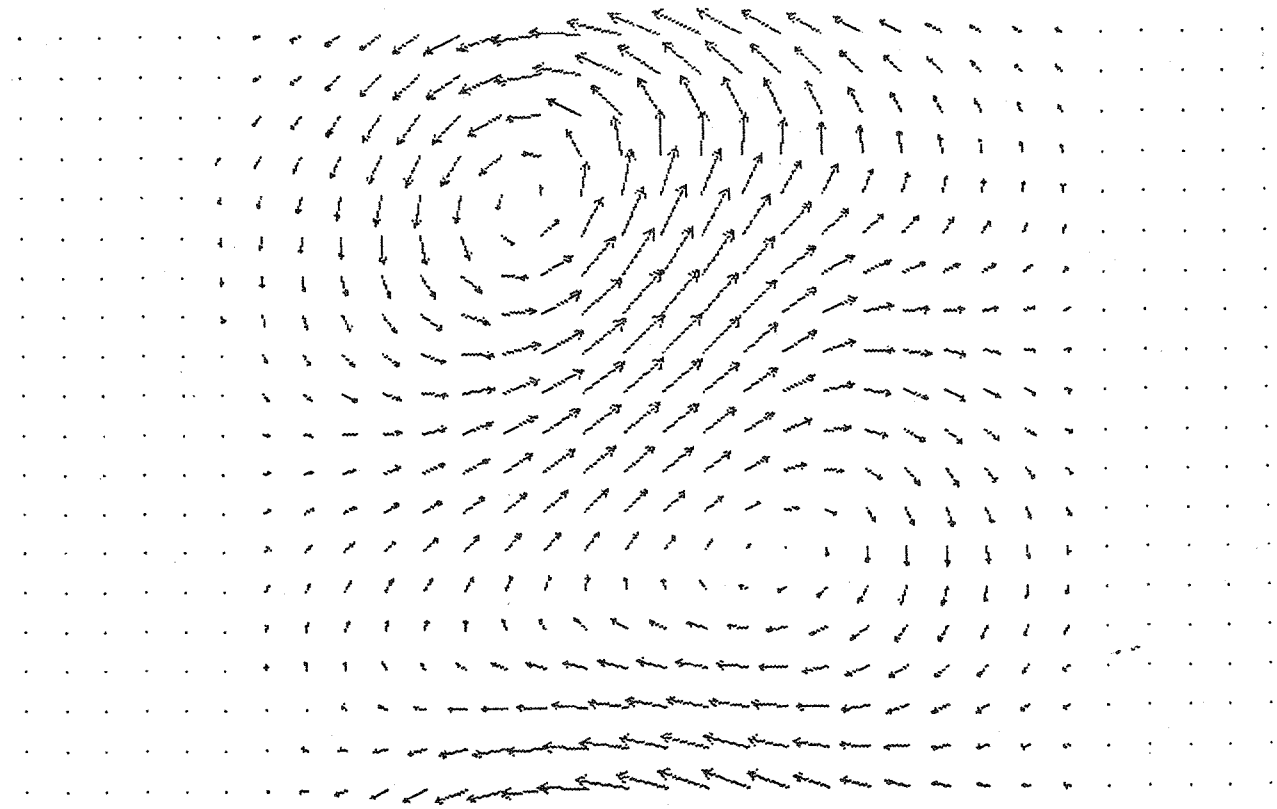

Fig. 4.10c Wind vector at $\sigma = .9$ day 6

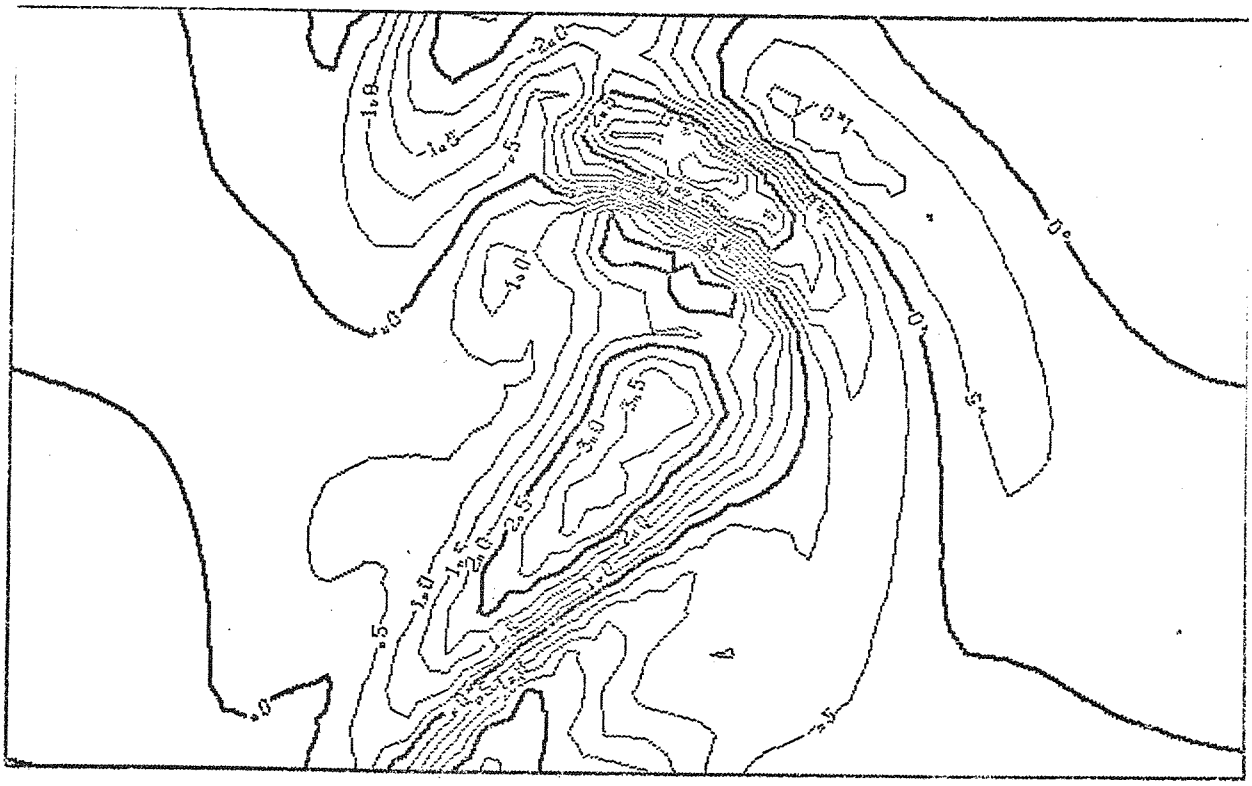

Fig.4.12 Divergence ($10^{-6}s^{-1}$) at σ=.7, day 6

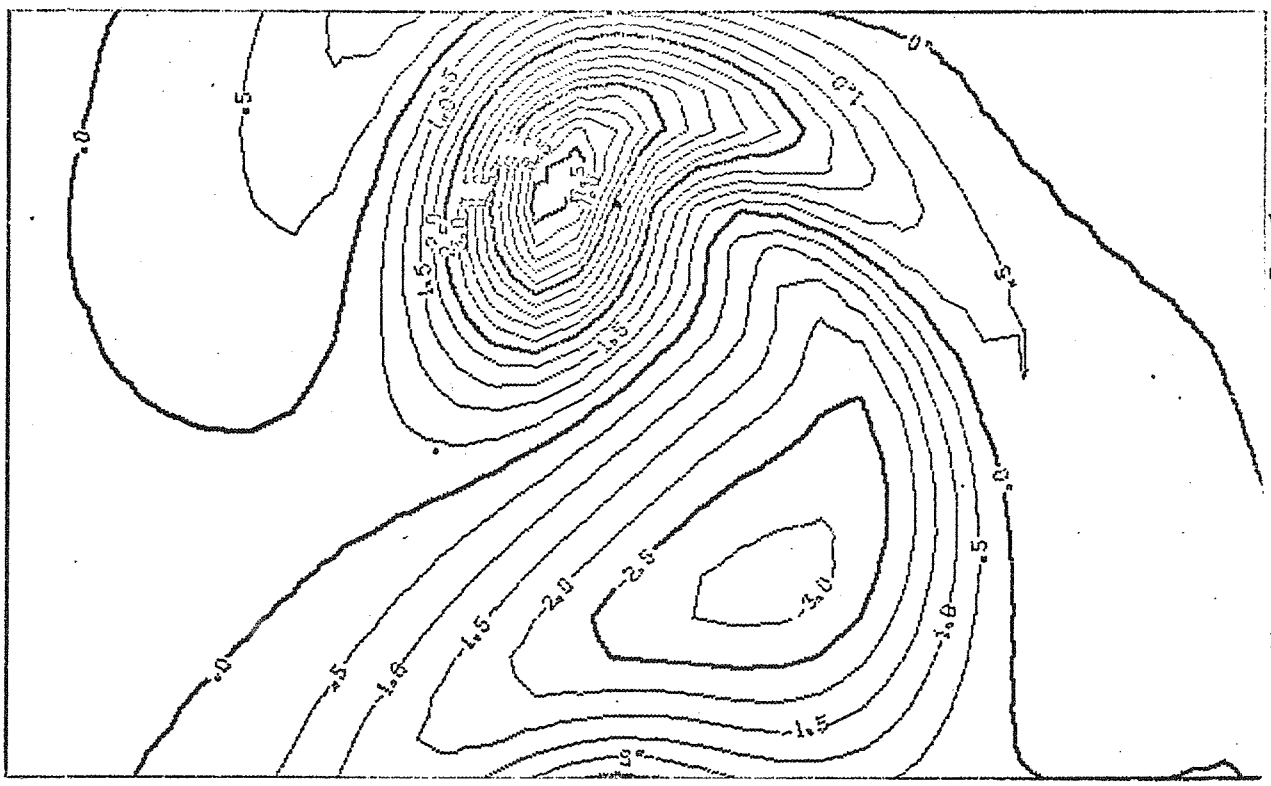

Fig. 4.11 Vorticity ($10^{-5}s^{-1}$) at σ=.9, day 6

5. Conclusions and further work

A channel version of the adiabatic part of the ECMWF gridpoint model has been developed. A few test integrations with low vertical resolution gave developments very similar to those reported in theoretical works with linearised model atmospheres. Both barotropically and baroclinically unstable waves have been examined, and they show many of the features observed in nature and described in the literature. A simulation of a short wavelength mid-latitude cyclone also produced realistic results.

Two particular difficulties have appeared in connection with the work. The method first chosen to produce initial fields proved to be ill-conditioned and limited the initial runs to low vertical resolution. This problem has now been overcome by another method of initialisation. The boundary conditions at the lateral walls in north and south produce noise in the form of slow divergent waves, generated close to the walls and moving perpendicularly into the region. This problem is still not overcome.
The channel model is now being extended to include a physics package, either the GFDL-package used in most of the Centre's global integrations, or the package developed at ECMWF. With the new version a series of high vertical resolution experiments will be done. In addition to the present monitoring of basic forecast parameters, energies and energy conversions will also be studied.

Acknowledgements

Thanks are expressed to Clive Temperton at ECMWF, who supplied the direct Poisson solver, and to David Burridge, also at ECMWF, for many discussions and suggestions.

References:

Burridge,D. & Haseler (1977) A model for medium range weather forecasts - Adiabatic formulation -.
ECMWF Technical Report No. 4 1977.

Haseler, J. & D. Burridge (1977) Documentation for the ECMWF gridpoint model.
ECMWF Internal Report No. 9 1977.

Hoskins, B. & A. Simmons (1975) A multi-layer spectral model and the semi-implicit method.
Quart.J.R.Met.Soc.(1975), 101, pp 637-655.

Kuo, H.L. (1949) Dynamic instability of two-dimensional divergent flow in a barotropic atmosphere.
J.Meteor., 6, 105-122.

Song, R.T. (1971) A numerical study of three-dimensional structure and energetics of unstable disturbances in zonal currents:Part I.
J.Atm.Sci.,Vol.28,(1971), pp. 549-564.

Yanai, M. & T. Nitta (1968) Finite difference approximations for the barotropic instability problem.
J.Met.Soc.Japan,Vol.46, (1968), pp.389-403.

EUROPEAN CENTRE FOR MEDIUM RANGE WEATHER FORECASTS
Research Department (RD)
Internal Report No. 16

No. 1 Users Guide for the GFDL Model (November 1976)

No. 2 The effect of Replacing Southern Hemispheric Analyses by Climatology on Medium Range Weather Forecasts (January 1977)

No. 3 Test of a Lateral Boundary Relaxation Scheme in a Barotropic Model (February 1977)

No. 4 Parameterization of the Surface Fluxes (February 1977)

No. 5 An Improved Algorithm for the Direct Solution of Poisson's Equation over Irregular Regions (February 1977)

No. 6 Comparative Extended Range Numerical Integrations with the ECMWF Global Forecasting Model 1: The N24, Non-Adiabatic Experiment (March 1977)

No. 7 The ECMWF Limited Area Model (March 1977)

No. 8 A Comprehensive Radiation Scheme designed for Fast Computation (May 1977)

No. 9 Documentation for the ECMWF Grid-Point Model (May 1977)

No. 10 Numerical Tests of Parameterization Schemes at an Actual Case of Transformation of Arctic Air (June 1977)

No. 11 Analysis Error Calculations for the FGGE (June 1977)

No. 12 Normal Modes of a Barotropic Version of the ECMWF Grid-Point Model (July 1977)

No. 13 Direct Methods for the Solution of the Discrete Poisson Equation: Some Comparisons (July 1977)

No. 14 On the FACR (ℓ) Algorithm for the Discrete Poisson Equation (September 1977)

No. 15 A Routine for Normal Mode Initialisation with Non-Linear Correction for a Multi-Level Spectral Model with Triangular Truncation (August 1977)

No. 16 A Channel Version of the ECMWF Grid-Point Model (December 1977)